SCIEPublish

Article

Metallurgical Characteristics of 316L Stainless Steel by Laser Additive Manufacturing

Chuan Sun *, Pengfei He, Zhenfeng Hu and Xiubing Liang

National Innovation Institute of Defense Technology, Academy of Military Science, Beijing 100071, China; hepengfei93@163.com (P.H.); hu_zhenfeng@sina.com (Z.H.); liangxb_d@163.com (X.L.)

* Corresponding author. E-mail: sunchuanyeah@163.com (C.S.)

Received: 22 July 2024; Accepted: 26 August 2024; Available online: 28 August 2024

ABSTRACT: Laser Additive Manufacturing (LAM), an avant-garde technology in manufacturing, harnesses the precision of laser energy to fabricate intricate parts through the meticulous process of melting and subsequently depositing layers of metal powders. Among the esteemed materials employed, 316L stainless steel (316L SS) stands out for its unparalleled corrosion resistance, exceptional high-temperature tolerance, and remarkable creep strength, making it a ubiquitous choice in the aerospace, medical, and nuclear power sectors. LAM has distinguished itself in the fabrication of intricate 316L SS components, yet enhancing the metallurgical bonding strength within these structures remains a pivotal area of ongoing research. This research endeavor delves into the intricate microstructure and mechanical properties that characterize the interface between the LAM-produced 316L SS cladding layer and its substrate, further investigating how varying laser energy densities (E) subtly influence these properties within the additive manufactured components. Remarkably, the interface region exhibits a tensile strength of 615.1 MPa, surpassing that of both the deposited layer and the substrate by 5.4% and 7.4% respectively, underscoring a robust bond between the two layers. This investigation not only sheds light on the unique process capabilities and performance merits of LAM in crafting 316L SS cladding layers but also pioneers novel approaches and conceptual frameworks for bolstering the metallurgical bonding strength of this esteemed material. As such, it constitutes a treasure trove of insights for subsequent research endeavors and practical applications across related disciplines.

Keywords: Laser additive manufacturing; Metallurgical bonding strength; Microstructure; Mechanical properties; 316L stainless steel

1. Introduction

Laser Additive Manufacturing (LAM), as a novel manufacturing process, employs high-energy-density laser beams to melt and deposit metal powders layer by layer, achieving the entire process from geometric design of parts to the production of complete components [1–3]. With the continuous development of technology, LAM is increasingly applied in aerospace, automotive manufacturing, medical devices, and other fields [4–6]. In these fields, there are extremely high requirements for metallurgical bonding strength of materials to ensure the mechanical properties and reliability of components [4,7,8]. Metallurgical bonding strength is one of the key indicators for evaluating the performance of materials in Laser Additive Manufacturing (LAM). It directly affects the overall mechanical properties, density, and reliability of the materials [9,10]. As one of the most commonly used stainless steel materials, 316L stainless steel (316L SS) exhibits outstanding performance in corrosion resistance, high-temperature resistance, and creep resistance, making it widely used in aerospace, medical, and nuclear power plant industries [11–13]. With the continuous expansion of application fields, the requirements for metallurgical bonding strength of 316L SS are also increasing. Compared with traditional processes such as casting and forging, LAM technology offers advantages such as flexible manufacturing processes, high material utilization rates, and the ability to produce complex structures [14–16]. Furthermore, LAM technology can effectively improve the metallurgical properties of materials by depositing different materials or compositions on the substrate surface. For 316L SS, LAM technology can deposit cladding layers with excellent corrosion resistance, high-temperature resistance, and creep resistance on its surface, thereby meeting the

https://doi.org/10.35534/ism.2024.10012

usage requirements under different working conditions [17–19]. Günen et al. [20] studied the effect of different heat treatment conditions (boronizing and homogenization heat treatment) on the wear resistance of ER307 stainless steel. The results showed that compared with the original samples, the wear resistance of the boronized ER307 stainless steel samples increased by 31.84 times and 8.06 times at room temperature and 500 °C, respectively. It indicates that homogenization and boronization treatment of stainless steel produced by arc welding additive manufacturing can improve friction properties. Li et al. [21] used a composite technology combining laser shock peening (LSP) and arc welding additive manufacturing to produce thin-walled AZ31 components. The residual stress state of the formed components and the microstructural evolution such as nanocrystallization and grain refinement in the nanocrystalline layer were analyzed. The results showed that this method successfully improved the corrosion resistance of the thin-walled AZ31 magnesium alloy components produced by arc welding additive manufacturing. However, in the additive manufacturing process, the microstructure and mechanical properties of the interface between the cladding layer and the substrate are crucial factors affecting the metallurgical bonding strength of the formed components. The microstructure, composition distribution, and interface bonding strength in the interface region can all influence the adhesion, corrosion resistance, and mechanical properties of the deposited layer [22–24]. An over-deposition method to suppress the formation of cracks was used by Oh et al. [25] during the additive manufacturing repair process. The mechanical properties of the repaired samples with different widths and heights of over-deposition volume were studied. The results showed that the tensile strength and elongation of the samples repaired using the over-deposition method were increased by 112% and 175%, respectively, compared to those of the samples repaired without over-deposition. An electrospark deposition (ESD) technique was utilized by Enrique et al. [26]. The results showed that a reduction in energy input during the ESD process led to the formation of more lamellar boundaries and higher yield strength during tensile testing. At low energy densities, there was no significant difference in yield strength between the repaired samples and the base material samples.

Currently, an extensive body of literature exists on laser-assisted rapid prototyping and repair remanufacturing of alloys, yet a notable void persists in the realm of systematic discourse concerning the interface dynamics between the laser cladding layer and the 316L SS substrate. The metallurgical bonding characteristics at this interface junction, pivotal for the integrity of laser-remanufactured components, necessitate urgent attention. The congruity and seamless transition of chemical compositions, microstructures, and properties across this interface significantly influence the operational efficacy and safety margins of the remanufactured parts. To bridge this gap and address these challenges head-on, the present study endeavors to fabricate 316L SS components utilizing LAM (Laser Additive Manufacturing) technology. It delves deeply into the microstructural nuances of the interface between the cladding layer and the substrate, while concurrently investigating the evolution of mechanical properties through rigorous tensile strength and hardness testing. This holistic approach not only furnishes a robust theoretical framework but also lays down an experimental groundwork, vital for resolving the aforementioned issues and advancing the field of laser-based repair and remanufacturing.

2. Experimental Methods

The LAM experiment of 316L SS was conducted on the laser additive manufacturing system consisting of an IPG YLS-2000 fiber laser, a five-axis manipulator, a powder feeder, and a computer. The laser can provide a continuous and stable laser beam with a power range of 2000 W and a wavelength of 1064 nm. The synchronous coaxial powder feeding method was adopted, using nitrogen as the powder carrier gas and protective gas. The gas flow rate was in a direct ratio to the powder feed rate, with a ratio of 1 L/min:1 g/min. The 316L powder was placed in the powder feeder, with a feed rate of 1–6 g/min. The LAM process is shown in Figure 1. The laser generates a stable high-energy laser beam, which is connected to the processing head through an optical fiber. The powder is connected to the processing head through a gas circuit. The processing head is fixed on the manipulator, which moves along the designed path. The laser beam melts the powder beam and moves synchronously to realize sample preparation. The substrate material is forged and aged 316L SS, with a substrate size of 100 mm × 100 mm × 20 mm. The composition of the substrate is shown in Table 1. Before the experiment, the upper surface of the substrate needs to be polished to remove the metal oxide layer and cleaned with alcohol. Gas-atomized 316L SS alloy powder was selected as the laser cladding powder, and its chemical composition is shown in Table 1.

The shape and particle size distribution of 316L SS powder were shown in Figure 2. As shown in Figure 2a, the shape of the 316L SS powder is spherical or near-spherical. According to the Figure 2b, the particle size distribution of the 316L SS powder tends to be normal, with a powder particle size ranging from 14 to 108 μm and an average particle

size of 56 μm. In the experiment, the inert gas used for both the powder feeder and the laser shielding gas was argon with a purity of 99.99%. Additionally, the 316L SS cladding powder was dried for 2 h before laser processing to remove surface moisture and avoid the presence of unevaporated water droplets in the cladding layer. The process parameters for LAM forming are as follows: laser power (P) ranging from 1000 to 2000 W, scanning speed (v) of 3–6 mm/s, laser spot diameter (D) of 3 mm, overlap rate of 40%, and Z-axis increment of 1 mm. The specific experimental parameters are shown in Table 2.

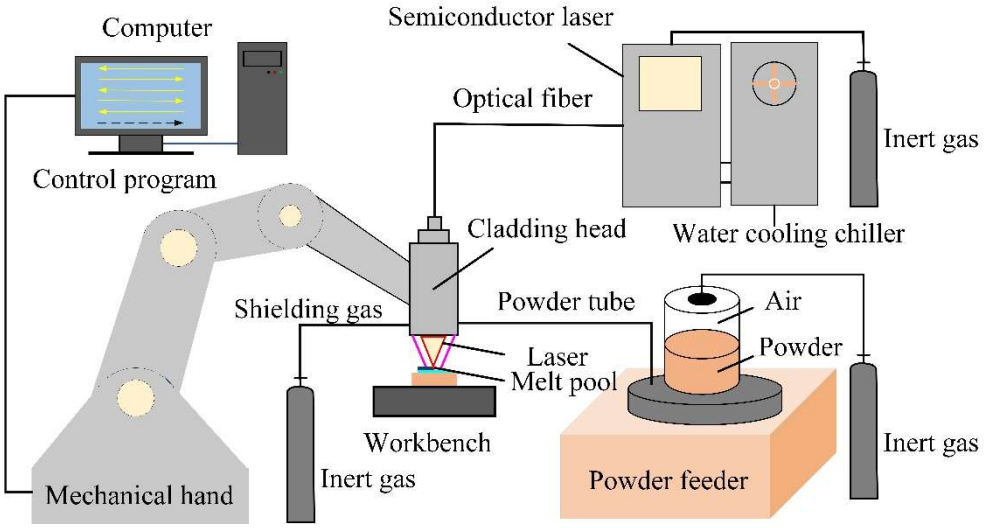

Figure 1. The equipment and forming process of laser additive manufacturing.

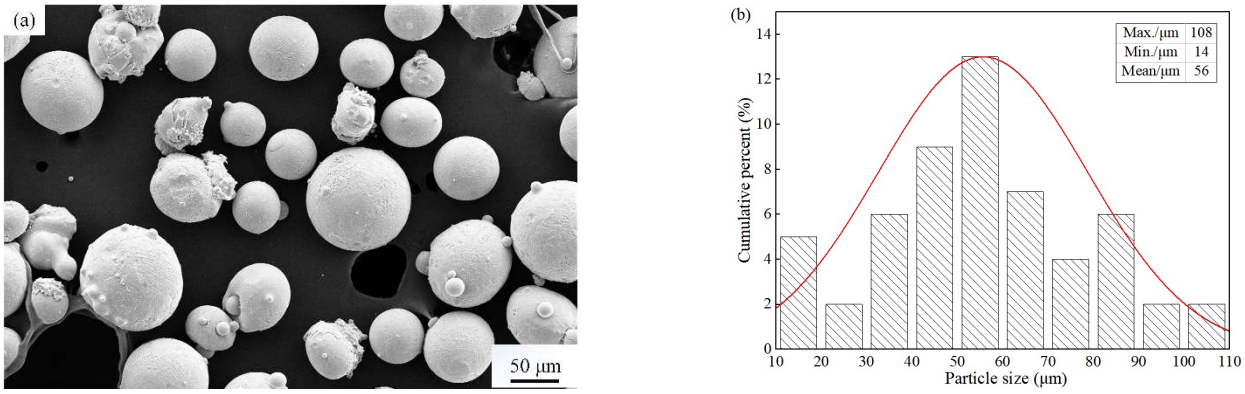

Figure 2. 316L SSl: (**a**) Powder shape under SEM and (**b**) Particle size distribution.

Table 1. Chemical Composition of 316L SS Alloy (wt%).

Element	C	Mn	Si	Cr	Ni	Mo	P/S	Fe
316L SS substrate	0.026	0.92	0.36	16.05	10.01	2.05	0.02	Bal.
316L SS powder	0.003	0.8	0.60	16.97	12.18	2.89	0.01	Bal.

Table 2. The process parameters of LAM.

Parameters	Unit	Value
Laser power	W	900, 1200, 1500
Scanning speed	mm/s	5
Powder feeding	g/min	1
Scanning space	mm	1
Spot diameter	mm	3
Layer thickness	mm	1
volume energy density	J/mm^3	180, 240, 300

Laser processing involves numerous process parameters, which increases the complexity of the forming process. To comprehensively analyze the impact of the processing technology, the volume energy density (E, J/mm^3) was used as an analytical parameter. E can be expressed as follows [27,28]:

$$E = P/\mathrm{d}hv \quad (1)$$

According to Equation (1), increasing the laser power or decreasing the scanning speed, scanning spacing, and layer thickness can increase the volume energy density. For the convenience of the experiment, the required laser energy density was obtained by varying the laser power alone.

A wire cutting machine was used to cut appropriate sized samples along the cross-section or longitudinal section of the formed part for metallographic sampling. Rinse the surface of the samples with anhydrous ethanol and wipe them clean. Then 320, 800, 1200, 2000, and 3000 grit sandpapers were used to polish the samples in sequence. When there are no obvious scratches on the surface of the sample, a polishing machine was utilized to polish the sample. Diamond polishing paste with a particle size of 2.5 μm was utilized to polish. Samples need to be confirmed without scratches and other defects under VHX-1000E ultra depth of field optical microscope. Corrosion was carried out using a solution consisting of 16 g $FeCl_3$ + 16 mL HCL + 32 mL H_2O [29,30]. After the sample is corroded, it needs to be washed with clean water immediately, and then washed with anhydrous ethanol and dried. The VHX-1000E ultra depth of field optical microscope was used to take metallographic photos of the samples. X-ray diffraction analyzer (XRD) was used to perform phase analysis on the surface of polished but uncorroded samples. The model is PANalytical X'Pert Pro, which is equipped with CuKa target material for phase analysis. The acceleration voltage, working current, scanning range, and scanning step were set to 40 kV, 40 mA, 20–80°, and 0.03 °/s, respectively [31,32]. The microhardness of 316L SS was measured using the HVS-1000 microhardness tester. According to the national standard GB/T4340.1-1999, a load of 200 g was selected and the holding time was 15 s [33,34]. 5 points at equal intervals were measured in the horizontal direction at each measurement position. The average value was the average microhardness of that measurement position. A room temperature tensile performance test was conducted on samples manufactured by laser additive manufacturing, using the HT5000 universal tensile testing machine with a tensile testing speed of 0.5 mm/s [35,36]. According to the national standard GB/T 228.1-2010 [37,38], the sampling location and specific dimensions of the tensile sample are shown in Figure 3. The tensile test samples along the laser scanning direction were cut by the wire cutting. 3 tensile test samples for each type of sample were prepared. The average value was used as the final result. The XRD data were analyzed by the spectrum, and the composition was determined by comparing the standard card. Calculate the mean value and standard deviation of hardness and tensile test data to ensure scientific and effective data.

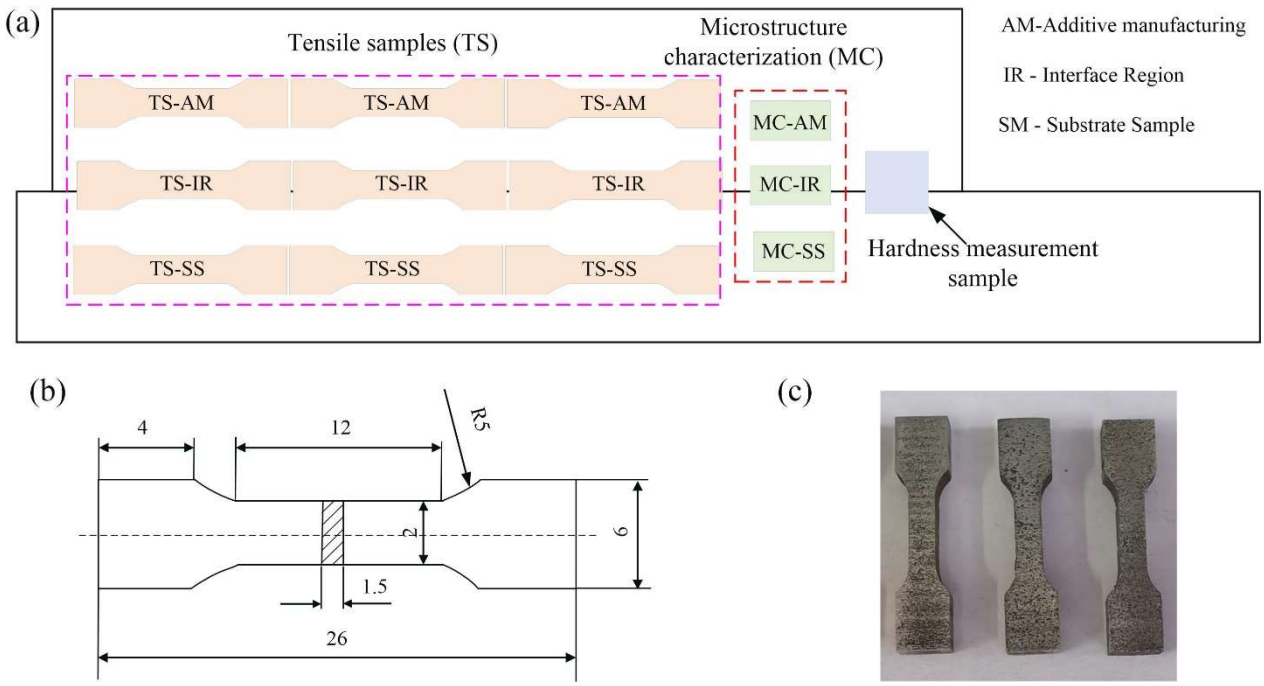

Figure 3. Schematic illustration: (**a**) The experimental procedure and their locations including tensile sample, microstructure characterization, and hardness measurement (**b**) Dimensions of tensile specimens, (**c**) The TS-AM fractured before the tests.

3. Experimental Results and Analysis

3.1. Phase Analysis

The X-ray diffraction pattern of laser cladding 316L SS alloy coating was shown in Figure 4. It indicates that the strong diffraction peaks of all samples (additive AM, interface IR, and substrate) correspond to the crystal planes (111), (200), and (220) of the face centered cubic (fcc) lattice, known as γ-Fe austenite [38–40]. Compared with the XRD pattern of 316L substrate (forged) parts, there is basically no shift in the peak positions. But it is not difficult to find that the peak intensity of the additive formed samples and the samples at the junction of the additive and the substrate are significantly weaker than those of the substrate components. The peak strength of additive formed parts is equivalent to the peak strength at the junction. There is a significant difference in the proportion of the three main peaks in the area of the sample, and the pattern that almost all show is: (111) > (200) > (220). Compared with the standard 2θ position of the γ-Fe phase (PDF # 31-0619). the 20 of the γ-Fe phase in this experiment showed a slightly higher Bragg angle, resulting in residual stress and corresponding lattice distortion. This may be caused by laser-induced thermal stress. Yang et al. [41] and Wang et al. [42] have both conducted similar reports.

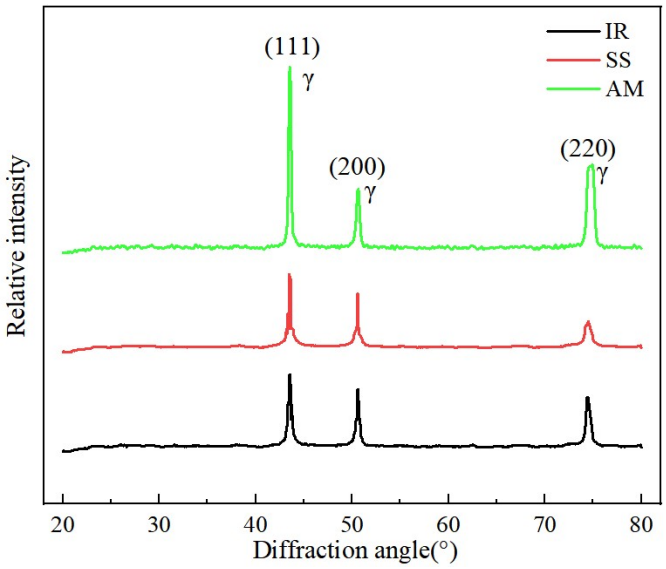

Figure 4. X-ray diffraction patterns of the deposition layer and substrate at different positions.

3.2. Characterization of Microstructure in the Interface Area

Laser additive manufacturing technology is an efficient and high-precision coating preparation method, particularly suitable for the preparation of 316L SS parts. This technology uses a high-energy-density laser beam to melt 316L SS alloy powder and deposit it on the substrate surface, forming a metallurgically bonded deposited layer. In the interface region between the deposited layer and the substrate, the microstructural characteristics have a significant impact on the performance of the deposited layer. The microstructural morphology of the region near the interface is shown in Figure 5b. The overall section included the heat affected zone of the substrate, the interface zone between the cladding layer and the substrate and the cladding zone. The cladding area was the area formed by the cladding material after laser melting and solidification, which is generally referred to as the cladding layer. It can be observed that the cladding region exhibits a typical dendritic crystal structure, which is attributed to the high energy density and rapid cooling process of energy sources such as lasers. The microstructures at different locations vary due to differences in material composition and heat dissipation conditions within the molten pool. The heat-affected zone appears brighter because the precipitated phase in this zone dissolves, significantly enhancing the corrosion resistance of the material and making it difficult for corrosive agents to corrode. The interface zone was a transition zone within the cladding region, containing both the composition of the cladding layer and a small amount of melted substrate composition. Therefore, the presence of this zone ensured the metallurgical bonding between the cladding layer and the substrate during the laser cladding process. There was a clear boundary between the cladding layer and the substrate, with alloy elements interchangeably dispersed and bonded. The bottom of the cladding layer microstructure exhibited characteristics of low-speed growth but lacks planar crystals, which is different from typical laser cladding microstructures. The organizational

continuity between the substrate and the cladding layer is stronger, which is beneficial for ensuring continuous mechanical properties and bonding strength. A good metallurgical bond was formed between the 316L SS alloy cladding zone and the substrate, with a clear interface and no obvious defects or cracks. The heat-affected zone of the substrate was the region where the substrate undergoes solid-state phase transformation due to the influence of thermal cycling. The microstructure near this zone was dense and grows in the direction opposite to the heat flow. This phenomenon occurred because the substrate material has good thermal conductivity, allowing heat to dissipate easily and resulting in a relatively high cooling rate. These analysis results indicated that the interface region between the 316L SS alloy cladding zone and the substrate exhibit excellent metallurgical bonding and microstructural characteristics, providing good mechanical properties, wear resistance, and corrosion resistance for the deposition layer.

The varying degrees of thermal history during laser additive manufacturing mainly include high cooling rates and large temperature gradients, which will directly affect the surface morphology and grain size of the formed parts [43,44]. Further analysis was conducted on the influence of different laser energy densities on the laser additive manufacturing of formed specimens, as shown in Figure 5a,d,e. The results indicate that when E was small, the molten pool had a high solidification rate, which results in insufficient gas escape time inside the molten pool, leading to the formation of pores inside the molten pool, as shown in Figure 5d. When E reached 240 J/mm^3, the melting state of the powder was good, and the weld channels tended to be fully overlapped. After solidification, the surface undulation was small, the forming quality was high, and the specimen had no obvious defects. With E increased to 300 J/mm^3, the temperature gradient of the melt pool was smaller, and the spreading time of the droplets was shorter than the solidification time, resulting in coarsening of the grains.

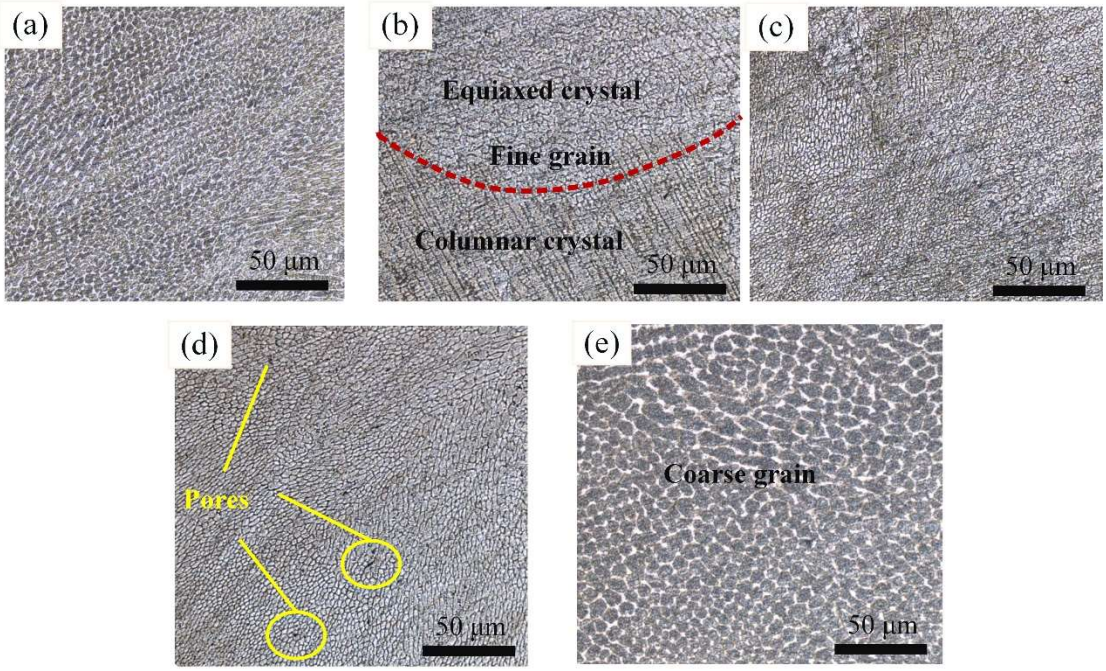

Figure 5. Microstructures with E = 240 J/mm^3 in different region: (**a**) LAM, (**b**) Interface, (**c**) Substrate, (**d**) E = 180 J/mm^3 in LAM, and (**e**) E = 300 J/mm^3 in LAM.

3.3. Characterization of Mechanical Properties in the Interface Region

To evaluate the influence of the interface region on hardness, the hardness was measured on the cross-section of the LAM-prepared sample. The hardness distribution in the interface region is shown in Figure 6. It indicated that the hardness of the substrate was approximately 260 HV. As the distance from the fusion line decreased, the hardness decreases, and the hardness of the heat-affected zone was slightly higher than that of the substrate. At a distance from the substrate, the hardness value of the heat-affected zone was relatively higher. This was because near the surface of the substrate, the cooling rate was higher due to the lower substrate temperature, resulting in finer grains in the microstructure. The hardness value at the cladding layer was lower than that of the substrate and the heat-affected zone, fluctuating within the range of 205–242 HV. Additionally, the influence of three different laser energy densities on the hardness of different regions was compared. The results indicated that when the laser energy density was 180 J/mm³, the heat-affected zone was the widest, and the hardness value was relatively larger, with the most significant increase

in hardness of the cladding layer. This is mainly due to the faster cooling rate of the grains in the cladding layer and finer grains at lower laser energy densities, where fine-grain strengthening plays a dominant role. When the energy density was 240 J/mm³ and 300 J/mm³, the heat-affected zone was narrower. At these three laser energy densities, the minimum hardness of the heat-affected zone was similar, and the hardness near the fusion line was also similar. For the deposited layer, the hardness value was higher in regions farther from the fusion line. Under different laser energy densities, the hardness value in the middle of the cladding layer did not vary significantly. This was mainly because the middle position of the molten pool was less affected by external factors and can solid-solve more elements such as Cr and Si during the solidification process, providing good solid-solution strengthening effects [45,46]. Due to convective and radiative heat dissipation mechanisms, the surface of the cladding layer cooled the fastest, resulting in the highest hardness value, closed to 242 HV. However, overall, the hardness values of the cladding layer did not differ significantly.

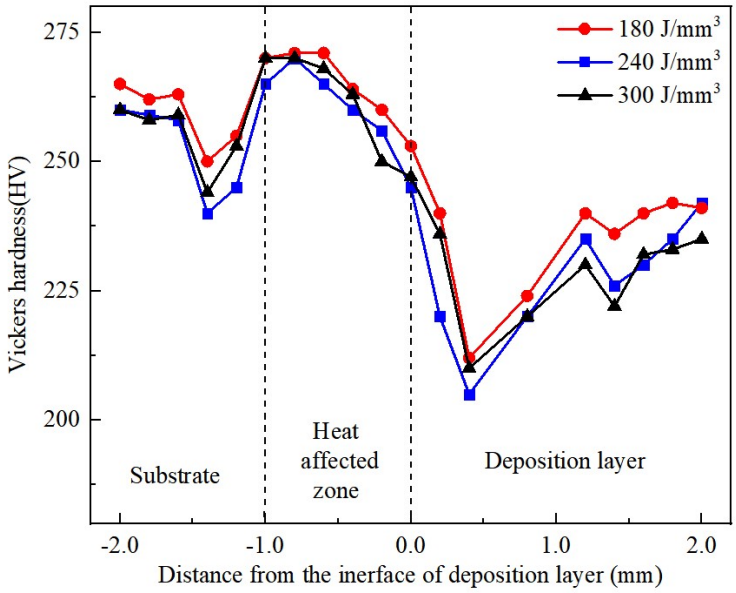

Figure 6. The hardness distribution of interface area.

To comprehensively understand the influence of the interface between the laser additive manufacturing (LAM) 316L SS cladding zone and the substrate on mechanical properties, tensile tests were conducted and analyzed. The tensile properties of LAM components under different laser energy densities and compares them with the mechanical properties obtained from different regions (substrate, interface region) are shown in Figure 7. The results indicated that with *E* increased from 180 to 300 J/mm³, the ultimate tensile strength (UTS) varied from 507.3 to 583.6 MPa, the yield strength (YS) varied from 338.5 to 350.4 MPa, and the elongation to failure (ETF) varied from 45.1% to 53.3%. With the increase in laser energy density, the UTS of the specimens showed a trend of first increasing and then decreasing. The main reason for this phenomenon is that when the laser energy density is low, after the stainless steel powder absorbs the energy of the laser beam, the amount of liquid phase in the molten pool is small, and the molten pool is discontinuous, causing a large amount of unmelted powder particles and gas to remain on the formed part [47,48]. Under loading, fractures are more likely to occur, resulting in relatively low UTS and YS but relatively high ETF, indicating higher plasticity under these conditions. When *E* was 240 J/mm³, the UTS and YS of the specimens were the highest, reaching 583.6 MPa and 350.4 MPa, respectively. Compared to when *E* was 180 J/mm³, the UTS and YS of the specimens increased by 8.4% and 2.5%, respectively. However, the ETF decreased slightly to the lowest value (45.1%). The reason for this is that when the laser energy density reaches a certain threshold, the powder in the molten pool melts to form a stable molten pool, allowing gas to escape promptly. This reduces the porosity of the formed specimens, significantly reduces crack defects, and gradually increases the overall tensile strength. As the laser energy density continued to increase, when *E* was 300 J/mm³, the UTS and YS of the specimens were the lowest, at 507.3 MPa and 338.5 MPa, respectively, and the ETF increased to 53.3%. This is because as *E* continues to increase, the formation process involves rapid cooling and heating, leading to increased local temperature gradients, forming a wider molten pool. After solidification, the volume contraction increases, and during the cooling and contraction process, it is subjected to resistance from the inner layers, resulting in increased residual stress. Considering the overall forming quality, when *E* was 240 J/mm³, the tensile strength of the LAM-formed specimens reached the optimal state, with UTS and YS of the specimens being 583.6 MPa and 350.4 MPa, respectively. The UTS and YS of LAM-formed 316L

samples are significantly higher than the industrial requirements for 316L [24], but the ETF decreases slightly. This is a very common characteristic of LAM-processed materials. The reason is that the higher cooling rate leads to a fine microstructure with high dislocation density, enhancing YS and UTS. However, metallurgical defects such as porosity, cracks, and unmelted powder particles inevitably occur, leading to reduced ductility. Further comparisons of the tensile properties across different regions were conducted. The results indicated that the average yield strength (YS) was highest in the substrate region (356.7 MPa), followed by the interface region (353.2 MPa) and the LAM specimens (350.4 MPa). However, the difference in YS between these regions was not significant (less than 5%). On the other hand, UTS was highest in the interface region (615.1 MPa), followed by the LAM components at 583.6 MPa. The substrate had the lowest UTS, at 572.6 MPa. This is because the samples from the interface region have a portion at the bottom of the deposited layer that includes the smallest grain size between the substrate and the fusion line, as well as part of the heat-affected zone. The tensile strength in the interface region is higher than that in the substrate region, indicating that the LAM process can significantly enhance the tensile strength of the substrate. This also confirms that the bonding between the substrate and the deposited layer is strong, and the deposition process is reliable and stable.

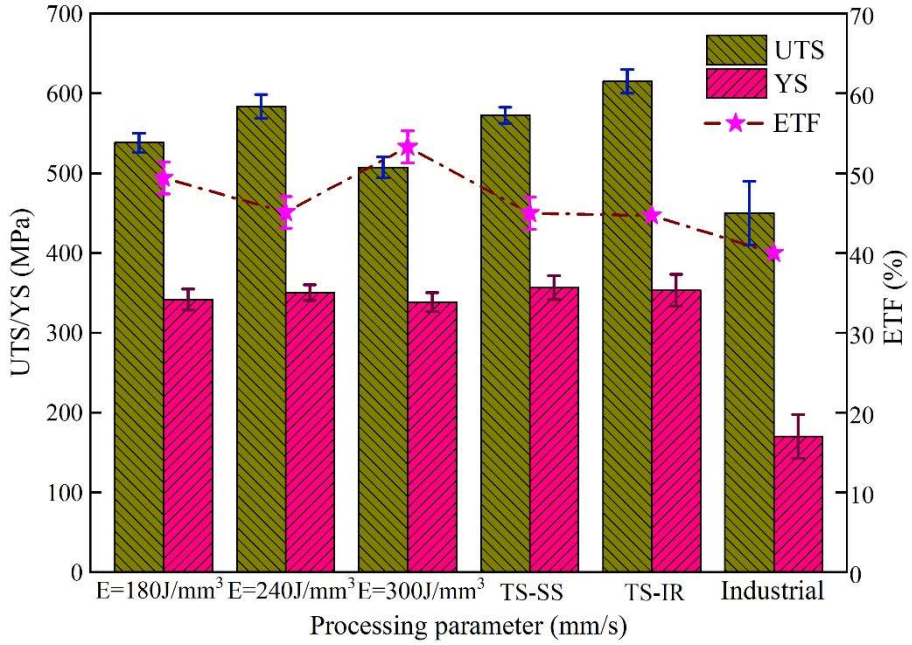

Figure 7. Comparison of tensile test results for conventional and LAM specimens with different regions.

The fracture morphologies of tensile samples from different regions were shown in Figure 8. It indicated that all fracture surfaces exhibited no obvious defects such as cracks or pores, indicating a dense microstructure of the samples. The nearly uniformly distributed dimple made observed on the fracture surfaces suggest that the fracture mechanism of all samples is ductile fracture. The relatively large grain size in the additive material resulted in larger and deeper dimples on the fracture surface of the additive sample, as shown in Figure 8a. Many unmelted spherical metal powder particles can also be observed, which are usually hidden in pits, indicating the presence of internal defects. These defects often lead to stress concentration, thereby accelerating the formation and propagation of microcracks into macroscopic cracks [49,50]. The reason for this is that during the process of LAM, the interaction between the laser beam and the metal powder and the melt, the movement of the metal powder, and the thermal capillary convection of the melt may all lead to the formation of pore defects, which can reduce the tensile properties of the formed parts [51,52]. On the other hand, due to the smaller grain size at the interface, shallow dimples were observed on the fracture surfaces, as shown in Figure 8b,c. All results indicate a strong bond between the additive material and the substrate, allowing them to work together as a single unit.

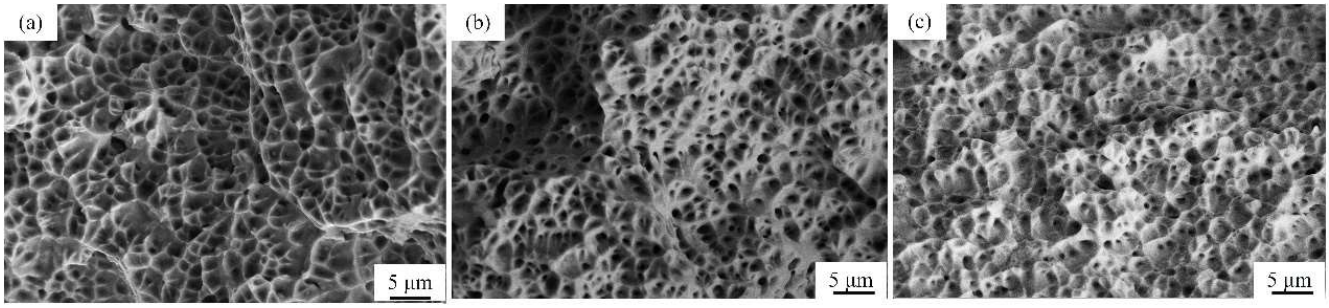

Figure 8. SEM images of the broken surfaces of the tensile samples: (**a**) AM-sample, (**b**) IR-sample, and (**c**) SS-sample.

4. Conclusions

This study employed LAM to fabricate 316L SS components. Specifically, a systematic analysis was conducted to investigate the impact of different regions on the microstructure and mechanical properties. Furthermore, the influence of varying laser energy densities on the LAM-fabricated components was analyzed, and the underlying mechanisms were elaborated and discussed in detail. The main conclusions were summarized as follows:

1. By ensuring the maintenance of optimal formation quality, a judicious elevation in laser energy density proves advantageous in narrowing the width of the heat-affected zone. The 316L SS alloy specimen crafted via LAM boasts a fusion line area characterized by a distinct, defect-free interface, devoid of cracks or imperfections. This underscores the exceptional metallurgical bonding and microstructural integrity at the interface between the deposition layer and the substrate, crucial for safeguarding both the fusion line's bonding strength and the uniformity of mechanical properties.
2. At a laser energy density of 240 J/mm³, the specimen attained peak values for ultimate tensile strength (UTS) at 583.6 MPa and yield strength (YS) at 350.4 MPa, respectively. Compared to a density of 180 J/mm³, these strengths witnessed an augmentation of 8.4% and 2.5%, respectively. Conversely, the elongation to failure (ETF) marginally declined to its nadir of 45.1%. This phenomenon can be attributed to the fact that as the laser energy density surpasses a threshold, the powder within the molten pool melds into a stable configuration, facilitating timely gas escape. This, in turn, mitigates porosity, significantly reduces crack defects, and progressively enhances the overall tensile strength of the specimen.
3. The IR-sample surpassed both the AM-sample and SS-sample in terms of both hardness and tensile strength. Notably, its peak hardness of 270 HV surpasses that of the AM-sample by 6.8% and the SS-sample by 17.1%. Similarly, its maximum tensile strength of 615.1 MPa exceeds the AM-sample by 5.4% and the SS-sample by 7.4%. These findings underscore the robust bonding performance between the additive material and the substrate. This study not only illuminates the process intricacies and performance advantages of LAM in crafting 316L SS deposited layers but also presents innovative strategies and concepts for bolstering the metallurgical bonding strength of 316L SS materials. Through the refinement of process parameters, precise modulation of the deposited layer's properties becomes feasible, catering to the diverse performance demands of 316L SS across various industries.

This study not only revealed the process characteristics and performance advantages of LAM in the preparation of 316L SS deposited layers, but also provided new methods and ideas for improving the metallurgical bonding strength of 316L SS materials. By optimizing process parameters, precise control over the properties of the deposited layers can be achieved, thereby meeting the demands of various industries for the performance of 316L SS.

Author Contributions

Conceptualization, C.S. and P.H.; Methodology, C.S.; Software, P.H.; Validation, C.S. and Z.H.; Formal Analysis, C.S.; Investigation, C.S. and P.H.; Resources, P.H.; Data Curation, P.H.; Writing—Original Draft Preparation, C.S.; Writing—Review & Editing, C.S. and X.L.; Visualization, X.L.; Supervision, X.L.; Project Administration, Z.H.; Funding Acquisition, C.S., X.L. and Z.H.

Ethics Statement

Not applicable.

Informed Consent Statement

Informed consent was obtained from all subjects involved in the study.

Funding

This research was funded by National Natural Science Foundation of China grant number No. 52022042, and Major National R&D Projects Foundation grant number No. J2019-VII−0008-0148.

Declaration of Competing Interest

The authors declare that they have no known competing financial interests or personal relationships that could have appeared to influence the work reported in this paper.

Data Availability

Data will be made available on request.

References

1. Korkmaz M, Gupta M, Robak G, Moj K, Krolczyk G, Kuntoglu M. Development of lattice structure with selective laser melting process: A state of the art on properties, future trends and challenges. *J. Manuf. Process* **2022**, *81*, 1040–1063.
2. Oliveira J, LaLonde A, Ma J. Processing parameters in laser powder bed fusion metal additive manufacturing. *Mater. Des.* **2020**, *193*, 108762.
3. Guo QL, Zhao C, Qu ML, Xiong LH, Hojjatzadeh S, Escano L, et al. In-situ full-field mapping of melt flow dynamics in laser metal additive manufacturing. *Add. Manuf.* **2020**, *31*, 100939.
4. Fu Y, Downey A, Yuan L, Zhang T, Pratt A, Balogun Y. Machine learning algorithms for defect detection in metal laser-based additive manufacturing: A review. *J. Manuf. Process* **2022**, *75*, 693–710.
5. Fayazfar H, Salarian M, Rogalsky A, Sarker D, Russo P, Paserin V, et al. A critical review of powder-based additive manufacturing of ferrous alloys: Process parameters, microstructure and mechanical properties. *Mater. Des.* **2018**, *144*, 98–128.
6. Zhu ZG, Hu ZH, Seet H, Liu TT, Liao WH, Ramamurty U, et al. Recent progress on the additive manufacturing of aluminum alloys and aluminum matrix composites: Microstructure, properties, and applications. *Int. J. Mach. Tool Manu.* **2023**, *190*, 104047.
7. Edwards P, Ramulu M. Fatigue performance evaluation of selective laser melted Ti-6Al-4V. *Mater. Sci. Eng. A* **2014**, *598*, 327–337.
8. Abdulhameed O, Al-Ahmari A, Ameen W, Mian S. Additive manufacturing: Challenges, trends, and applications. *Adv. Mech. Eng.* **2019**, *11*, 1–27.
9. Wang YM, Voisin T, McKeown JT, Ye JC, Calta NP, Li Z, et al. Additively manufactured hierarchical stainless steels with high strength and ductility. *Nat. Mater.* **2021**, *17*, 63–71.
10. Gokuldoss PK, Kolla S, Eckert J. Additive manufacturing processes: Selective laser melting, electron beam melting and binder jetting-selection guidelines. *Materials* **2017**, *10*, 672.
11. Zhan ZX, Li H, MachGuo QL, Zhao C, Qu ML, Xiong LH, et al. In-situ characterization and quantification of melt pool variation under constant input energy density in laser powder bed fusion additive manufacturing process. *Add. Manuf.* **2019**, *28*, 600–609.
12. Cherry JA, Davies HM, Mehmood S, Lavery NP, Brown SGR, Sienz J. Investigation into the effect of process parameters on microstructural and physical properties of 316L stainless steel parts by selective laser melting. *Int. J. Adv. Manuf. Technol.* **2015**, *76*, 869–879.
13. Gu D, Shi X, Poprawe R, Bourell D, Setchi R, Zhu J. Material-structure-performance integrated laser-metal additive manufacturing. *Science* **2021**, *372*, 932.
14. Nadammal N, Mishurova T, Fritsch T, Serrano-Munoz I, Kromm A, Haberland C, et al. Critical role of scan strategies on the development of microstructure, texture, and residual stresses during laser powder bed fusion additive manufacturing. *Add. Manuf.* **2021**, *38*, 101792.
15. Svetlizky D, Das M, Zheng BL, Vyatskikh AL, Bose S, Bandyopadhyay A, et al. Directed energy deposition (DED) additive manufacturing: Physical characteristics, defects, challenges and applications. *Mater. Today* **2021**, *49*, 271–295.
16. Sing SL, An J, Yeong WY, Wiria FE. Laser and electron-beam powder-bed additive manufacturing of metallic implants: A review on processes, materials and designs. *J. Orthop. Res.* **2016**, *34*, 369–385.
17. Casati R, Lemke J, Vedani M. Microstructure and Fracture Behavior of 316L Austenitic Stainless Steel Produced by Selective Laser Melting. *J. Mater. Sci. Technol.* **2016**, *32*, 738–744.
18. Ahn DG. Directed Energy Deposition (DED) Process: State of the Art. *Int. J. Precis. Eng. Man-GT* **2021**, *8*, 703–742.

19. Bertsch KM, de Bellefon GM, Kuehl B, Thoma DJ. Origin of dislocation structures in an additively manufactured austenitic stainless steel 316L. *Acta Mater*. **2020**, *199*, 19–33.
20. Günen A, Gürol U, Koçak M, Çam G. A new approach to improve some properties of wire arc additively manufactured stainless steel components: Simultaneous homogenization and boriding. *Surf. Coat. Tech.* **2023**, *460*, 129395.
21. Li XZ, Fang XW, Zhang MG, Zhang HK, Duan YS, Huang K. Gradient microstructure and prominent performance of wire-arc directed energy deposited magnesium alloy via laser shock peening. *Int. J. Mach. Tool. Manu.* **2023**, *188*, 104029.
22. He SS, Park S, Shim D, Yao CL, Li MC, Wang SL. Effect of substrate preheating on the microstructure and bending behavior of WC-Inconel 718 composite coating synthesized via laser directed energy deposition. *Int. J. Refract Met. H* **2023**, *115*, 106299.
23. Sun ZJ, Tan XP, Tor SB, Yeong WY. Selective laser melting of stainless steel 316L with low porosity and high build rates. *Mater Des.* **2016**, *104*, 197–204.
24. Liu TS, Chen P, Qiu F, Yang HY, Jin NTY, Chew YX, et al. Review on laser directed energy deposited aluminum alloys. *Int. J. Extrem. Manuf.* **2024**, *6*, 022004.
25. Oh WJ, Son JY, Baek GY, Shim D. Excess deposition for suppressing interfacial defects induced on parts repaired using direct energy deposition. *Int. J. Adv. Manuf. Technol.* **2020**, *106*, 1303–1316.
26. Enrique PD, Jiao Z, Zhou NY, Toyserkani E. Effect of microstructure on tensile properties of electrospark deposition repaired Ni-superalloy. *Mat. Sci. Eng. A-Struct* **2018**, *729*, 268–275.
27. Gong YD, Yang YY, Qu SS, Li PF, Liang CY, Zhang H. Laser energy density dependence of performance in additive/subtractive hybrid manufacturing of 316L stainless steel. *Int. J. Adv. Manuf. Technol.* **2019**, *105*, 1585–1596.
28. Li C, Wang YP, Ma SY, Yang XS, Li JF, Zhou YZ, et al. Densification, microstructural evolutions of 90W-7Ni-3Fe tungsten heavy alloys during laser melting deposition process. *Int. J. Refract Met. H* **2020**, *91*, 105254.
29. Yahyaoui H, Ben Moussa N, Habibi M, Ghanem F, Ben Salah N. Improvement of corrosion resistance of additive manufactured AISI 316L stainless steel in a physiological environment by TiN surface coating. *Int. J. Adv. Manuf. Technol.* **2023**, *125*, 2379–2391.
30. Yang YY, Gong YD, Qu SS, Rong YL, Sun Y, Cai M. Densification, surface morphology, microstructure and mechanical properties of 316L fabricated by hybrid manufacturing. *Int. J. Adv. Manuf. Technol.* **2018**, *97*, 2687–2696.
31. Mao H, Jing CC, Kong FX, Xu TQ, Xiao X, Li K, et al. Improve the manufacturing efficiency of steel bars by using hot-wire pulse arc additive manufacturing. *J. Manuf. Process* **2023**, *89*, 430–443.
32. Qu S, Gong Y. Effect of heat treatment on microstructure and mechanical characteristics of 316L stainless steel parts fabricated by hybrid additive and subtractive process. *Int. J. Adv. Manuf. Technol.* **2021**, *117*, 3465–3475.
33. Hsu HC, Wong KK, Wu SC, Hou PJ, Ho WF. Effects of heat treatment through muffle furnace or microwave on microstructure and corrosion behavior of 316L stainless steel produced by selective laser melting. *Mrs. Commun.* **2023**, *13*, 177–183.
34. Wang Q, Zhang S, Zhang C, Wu C, Wang J, Chen J, Sun Z. Microstructure evolution and EBSD analysis of a graded steel fabricated by laser additive manufacturing. *Vacuum* **2017,** *141*, 68–81.
35. Xu WW, Wang C, Long Y, Li CJ, Li GX, Ding SL. The influence of deformation affected region on microstructure and mechanical property of 316L fabricated by hybrid additive-subtractive manufacturing. *J. Manuf. Process* **2024**, *117*, 154–169.
36. Kannan AR, Kumar SM, Pramod R, Shanmugam NS, Vishnukumar M, Naveenkumar S. Microstructural characterization and mechanical integrity of stainless steel 316L clad layers deposited via wire arc additive manufacturing for nuclear applications. *Mater. Werkst* **2021**, *52*, 617–623.
37. Wang XH, Wu YM, Sun L, Hu CH, Li Z, Liu LM, et al. Microstructure Evolution and Mechanical Properties of Ferrite–Austenite Stainless Steel Bimetals Fabricated via Wire Arc Additive Manufacturing. *Steel Res. Int.* **2024**, *95*, 2300494.
38. Yang YY, Gong YD, Qu SS, Xie HL, Cai M, Xu YC. Densification, mechanical behaviors, and machining characteristics of 316L stainless steel in hybrid additive/subtractive manufacturing. *Int. J. Adv. Manuf. Technol.* **2020**, *107*, 177–189.
39. Jeyaprakash N, Kumar MS, Yang CH, Cheng YH, Radhika N, Sivasankaran S. Effect of microstructural evolution during melt pool formation on nano-mechanical properties in LPBF based SS316L parts. *J. Alloys Compd.* **2024**, *972*, 172745.
40. Xu QZ, Jiang DW, Zhou J, Qiu ZH, Yang X. Enhanced corrosion resistance of laser additive manufactured 316L stainless steel by ultrasonic surface rolling process. *Surf. Coat. Tech.* **2023**, *454*, 129187.
41. Yang YY, Gong YD, Li CH, Wen XL, Sun JY. Mechanical performance of 316 L stainless steel by hybrid directed energy deposition and thermal milling process. *J. Mater. Process Tech.* **2021**, *291*, 117023.
42. Wang D, Song CH, Yang YQ, Bai YC. Investigation of crystal growth mechanism during selective laser melting and mechanical property characterization of 316L stainless steel parts. *Mater. Des.* **2016**, *100*, 291–299.
43. Carroll BE, Otis RA, Borgonia JP, Suh JO, Dillon RP, Shapiro AA, et al. Functionally graded material of 304L stainless steel and inconel 625 fabricated by directed energy deposition: Characterization and thermodynamic modeling. Acta Mater **2016**, *108*, 46–54.
44. Xiao LJ, Xu X, Feng GZ, Li S, Song WD, Jiang ZX. Compressive performance and energy absorption of additively manufactured metallic hybrid lattice structures. *Int. J. Mech. Sci.* **2022**, *219*, 107093.
45. Wei C, Li L. Recent progress and scientific challenges in multi-material additive manufacturing via laser-based powder bed fusion. *Virtual Phys. Prototy* **2021**, *16*, 347–371.

46. Sun C, Wang Y, McMurtrey MD, Jerred ND, Liou F, Li J. Additive manufacturing for energy: A review. *Appl. Energ.* **2021**, *282*, 116041.
47. Bertoli US, Wolfer AJ, Matthews M, Delplanque JP, Schoenung JM. On the limitations of Volumetric Energy Density as a design parameter for Selective Laser Melting. *Mater Des.* **2017**, *113*, 331–340.
48. Ghayoor M, Lee K, He YJ, Chang CH, Paul BK, Pasebani S. Selective laser melting of 304L stainless steel: Role of volumetric energy density on the microstructure, texture and mechanical properties. *Add. Manuf.* **2020**, *32*, 101011.
49. Lian ZX, Zhou JH, Ren WF, Chen FZ, Xu JK, Tian YL, et al. Recent progress in bio-inspired macrostructure array materials with special wettability-from surface engineering to functional applications. *Int. J. Extrem. Manuf.* **2024**, *6*, 012008.
50. Ibrahim B, Lopez L, Kulkarni S, Jobes D, Forgiarini M, Barber JR, et al. Increasing strength properties in sinter-based additive manufacturing of SS316L via metal material jetting of sub-micron powders. *Add. Manuf.* **2024**, *89*, 104268.
51. Shi YX, Zhao B, Ding WF. Solid additives to increase the service life of ceramic cutting tool: Methodology and mechanism. *Intell. Sustain. Manuf.* **2024**, *1*, 10009.
52. Gu G, Wang DZ, Wu SJ, Zhou S, Zhang BX. Research Status and Prospect of Ultrasonic Vibration and Minimum Quantity Lubrication Processing of Nickel-based Alloys. *Intell. Sustain. Manuf.* **2024**, *1*, 10006.